CERN-LHCC-2006-034
LHCC-RD-011
RD Status Report/RD39
24 November 2006

RD39 STATUS REPORT 2006

CERN RD39 Collaboration

X.Rouby[j], P. Anbinderis[m], T. Anbinderis[m], N. D'Ambrosio[k],
R. Bates[e], W. de Boer[h], H.Bol[h], E. Borchi[c], M. Bruzzi[c], S. Buontempo[k], C. Buttar[e],
W. Chen[b], V. Cindro[i], V. Eremin[l], A. Furgeri[h], E. Gaubas[m], E. Grigoriev[d],
J. Härkönen[g], E. Heijne[a], S. Heising[h], I. Ilyashenko[l],
V. Kalesinskas[m], M. Krause[h], Z. Li[b], P. Luukka[g],
I. Mandic[i], D. Menichelli[c], M. Mikuz[i], O. Militaru[j], S. Mueller[h], T.O. Niinikoski[a],
V. O'Shea[e], S. Pagano[k], C. Parkes[e], K. Piotrzkowski[j], S. Pirollo[c], P. Pusa[f]
S. Reinhardt[h], J. Räisänen[f], E. Tuominen[g], E. Tuovinen[g],
J. Vaitkus[m], E. Verbitskaya[l], S. Väyrynen[f], M. Zavrtanik[i]

[a]CERN, CH-1211 Geneva, Switzerland
[b]Brookhaven National Laboratory, Upton, NY 11973-5000, USA
[c]Dipartimento di Energetica, Universitá di Firenze, I-50139 Firenze, Italy
[d]Department de radiologie, Université de Geneve, CH-1211 Geneve, Switherland
[e]Department of Physics and Astronomy, University of Glasgow, Glasgow G12 8QQ, United Kingdom
[f]Accelerator Laboratory, University of Helsinki, 00014 University of Helsinki, Finland
[g]Helsinki Institute of Physics, 00014 University of Helsinki, Finland
[h]IEKP University of Karlsruhe, D-76128 Karlsruhe, Germany
[i]Jozef Stefan Institute, Experimental Particle Physics Department, 1001 Ljubljana, Slovenia
[j]Université Catholique de Louvain, FYNU, Louvain-la-Neuve, Belgique
[k]Dipartimento di Fisica, Università degli Studi di Salerno and INFN, I-84081 Baronissi (SA), Italy
[l]Ioffe Physico-Technical Institute, Russian Academy of Sciences, St.Petersburg 194021, Russia
[m]University of Vilnius, Institute of Materials Science and Applied Research, 2040 Vilnius, Lithuania

Summary

CERN RD39 Collaboration is aiming for development of super-radiation hard cryogenic silicon detectors for applications of LHC experiments and their future upgrades. Radiation hardness up to 1×10^{16} n_{eq}/cm^2 is required in the future HEP experiments. The most important measure of the detector's radiation hardness is the Charge Collection Efficiency (CCE), which is affected by both the detector sensitive volume (depletion depth) and charge trapping by radiation-induced trapping centers. However, 1×10^{16} n_{eq}/cm^2 fluence is well beyond the radiation tolerance of even the most advanced semiconductor detectors fabricated by commonly adopted technologies. First, the full depletion voltage (V_{fd}) will be in the thousands of volts for a 300 μm thick Si detector operated at or near room temperature. Second, the charge carrier trapping will limit the charge collection depth to an effective range of 20 μm to 30 μm regardless of depletion depth. In order to maintain an acceptable CCE under Super LHC radiation environment, one has to solve both problems simultaneously.

The CERN RD39 Collaboration has launched in 2005 a project to build Transient Current Technique (TCT) and Charge Collection Efficiency (CCE) set-ups at CERN with temperature range from 35 K to 300 K (C-TCT). The C-TCT project was successfully completed in 2006. From TCT data it is possible to extract the full depletion voltage, effective trapping time, electric field distribution and the sign of the space charge in the silicon bulk. The interest in the extension of the temperature range down to helium temperatures is not only in the Super LHC tracker detectors, but also in the basic understanding of heavily radiation-damaged silicon. Our first results show that the trapping time constant increases and the V_{fd} decreases at the temperatures below 200K.

We have developed the advanced radiation hard detectors using charge or current injection, the current injected detectors (CID). In a CID, the electric field is controlled by injected current, which is limited by the space charge. This leads to nearly uniform electric field through the detector at any operating voltage regardless of the radiation fluence. The charge collected in 300 μm thick CID at 1×10^{16} n_{eq}/cm^2 is estimated to be equivalent of 1360 electrons at the 300V bias. This is close to standard detector hypothetically fully depleted with thousands of volts. An important advantage of CID is that at some given operating voltage, the current decreases with increasing irradiation fluence. This would result in segmented detector decreasing shot noise with respect of increasing fluence. With CID concept it is additionally possible to increase the absolute value of the colleted charge when the concentration of active trapping centers is reduced by cooling down to cryogenic temperatures. The CID's current-voltage and CCE properties have been confirmed in 2006 by many independent measurements.

1. Introduction

The radiation hardness studies have up to now been greatly focused to improve the (or reduce) of the detector full depletion voltage [1], which leads to the increase of detector sensitive volume and therefore the detector charge collection efficiency (CCE). This remains true if the level of radiation environment is in the order of 1×10^{15} n_{eq}/cm^2., when the trapping of carriers by radiation-induced defects are not dramatic (< 50%). However, for LHC upgrade, the SLHC, the expected radiation level will be 10 time higher, up to 1×10^{16} n_{eq}/cm^2. In this case, in addition to the detector full depletion problem, the trapping problem is the main limiting factor of CCE.

The total charge collected by a detector, Q, can be considered to be a product of two terms [2].

$$Q = Q_0 \cdot CCE_{GF} \cdot CCE_t = Q_0 \cdot \frac{w}{d} \cdot \frac{\tau_t}{t_{dr}}(1 - e^{-t_{dr}/\tau_t}) \qquad (1)$$

and Q_0 is the total charge deposited by a MIP particle in a detector of the thickness of d:

$$Q_0 = 80 \cdot d \text{ (electrons, here } d \text{ is in } \mu m) \qquad (2)$$

where w is the depletion depth, d the detector thickness, τ_t the trapping time constant, and t_{dr} the carrier draft time in the depletion region (i.e. $w = V_{dr}\, t_{dr}$, here is the carrier drift velocity). In Eq. 1, CCE_{GF} is a geometrical factor that is affected by detector full depletion voltage V_{fd} (or effective doping concentration N_{eff}) via the relations:

$$w = \sqrt{\frac{2\varepsilon\varepsilon_0 V}{eN_{eff}}} \text{ and } \frac{w}{d} = \sqrt{\frac{V}{V_{fd}}}\ , \qquad (3)$$

where e and ε have their usual meanings. The second term CCE_t in Eq. 1 is the trapping factor that is related to the trapping of carriers by defects.

Obviously, to increase CCE, one has to increase CCE_G and CCE_t simultaneously. This is particularly true for SLHC fluences at which the trapping term becomes the limiting factor for CCE as we will discuss below.

The trapping (τ_t) and detrapping (τ_d) time constants for a trap level can defined by:

$$\begin{cases} \tau_t = \dfrac{1}{\sigma v_{th} N_t} \\ \tau_d = \dfrac{1}{\sigma v_{th} N_C e^{-E_t/kT}} \end{cases} \qquad (4)$$

where σ is the capture cross section of the trap, v_{th} is the thermal velocity of charge

carriers, N_T is the concentration of traps, N_C the electric state density in the conduction band and E_t the trap energy level in the band gap.

The trapping time constant is nearly independent on temperature (or weak dependence on T). However, it depends strongly on the radiation fluence Φ_n. At a fluence of 1×10^{16} n_{eq}/cm^2, the trapping time can be as short as 0.2 ns [2]. Due to the effect of saturation of carrier drift velocity at about $V_s=10^7$ cm/s, the carrier drift time t_d is greater than 3 ns for a fully depleted 300 μm thick detector. In this case, Eq. (1) can be simplified as (also using Eq. (2), and $w= V_{dr}\, t_{dr}$):

$$Q \cong Q_0 \cdot \frac{w}{d} \cdot \frac{\tau_t}{t_{dr}} = 80 \cdot w \cdot \frac{\tau_t}{t_{dr}} = 80 \cdot V_{dr} \cdot \tau_t \qquad \text{electrons } (V_{dr}\, t_{dr} \text{ in } \mu\text{m}) \qquad (5)$$

We can define a charge collection distance l_{CCE} as:

$$l_{CCE} \equiv V_{dr} \cdot \tau_t \quad (\mu\text{m}) \qquad (6)$$

Then Eq. (5) can be re-written as the following:

$$Q \cong 80 \cdot l_{CCE} \text{ electrons} \quad (l_{CCE} \text{ in } \mu\text{m}) \qquad (7)$$

We note here that for SLHC fluences: 1) the total charge collected Q by a detector has no explicit dependence on the detector thickness; 2) the charge collection distance

$$l_{CCE} < V_S \cdot \tau_t \qquad (8)$$

which is about 20 μm for SLHC fluence of 1×10^{16} n_{eq}/cm^2., and the charge collected Q by a detector is about 1600 electrons, regardless of the detector thickness (for d > 20 μm)! Therefore the effective detector thickness for CCE is the charge collection distance l_{CCE}. Thus At a fluence of 1×10^{16} n_{eq}/cm^2, >90% of the detector volume (for a typical thickness of 200-300 μm) would represent an effective dead space.

As demonstrated by the previous RD39 results [3], the CCE_{GF} can be increased close to 1 by manipulating the electric field in the detector via current and/or charge injection at temperatures from 130 K to 150 K. Since for fluence less than 1×10^{15} n/cm^2, the trapping term CCE_t is relatively insignificant, CCE can be significantly improved by improving only the CCE_{GF} at temperatures from 130 K to 150 K. However, for extremely high fluence in LHC upgrade environment, as we discussed above, the trapping term will be significant and affect the CCE greatly. The approach of RD39 to overcome the fundamental trapping problem at very high fluencies is to modify the CCE_t at the low temperatures. The key of our approach is to use freeze-out of the trapping that affects charge collection efficiency (CCE). Temperatures lower than the 80 K may be needed

here. Table I lists four possible solutions for silicon detectors to be used in the most inner region of the SLHC.

Table 1 Silicon detector solutions for SLHC's most inner region

Solution	CCE improvement due to	Technology/ implementation difficulties
Replacement every 1-2 years	**New detectors**	**Hard to access the inner region**
3D Si detectors	**Small V_{fd}** **Small drift distance *t***	**Complicated processing technology** **Column spacing *t* should be < 40 μm** **Possible surface damage problem to ionizing radiation**
Cryogenic Si detectors	**Fixed electric field (small bias)** **Freezing traps (low trapping)** **Low leakage current**	**Difficult to implement cryogenic system**
Elevated temp annealing (DRIVE) **(MCZ Si only)**	**Annealing out of defect levels related to:** **Leakage current, space charges And trapping**	**Difficult to implement annealing in a full detector system**

As it can be seen in Table I, while all possible solutions for detectors in SLHC face some technology difficulties, the RD39 approach with cryogenic Si detectors is the only one that can possibly solve both the problems of charge collection and leakage current.

2. Cryogenic Transient Current Technique (C-TCT) project

The Transient Current Technique measurement is based on the detection of the dominant type of charge carrier, electron or hole, which drifts across the whole detector thickness after being excited by a photon. This is achieved by illuminating the front (n^+ implant) or back (p^+ implant) side of the detector with a laser, whose light creates electron-hole pairs close to the device surface. When the front-side of the detector is illuminated, the electrons are gathered to the n^+-electrode so fast that the signal is damped by the rise-time of the data acquisition electronics and therefore the measured signal is mainly coming from the holes that travel a longer distance through the silicon bulk. Correspondingly, when a $p^+/n^-/n^+$ detectors front side is illuminated, mainly the electron current is measured [4,5].

Depending on the space charge of the bulk, the electric field i.e. the collecting junction is either on the front side or the back side of the detector. When measured from the front side, if the junction is on the front side, a descending hole transient current is measured. If the junction is on the back side i.e. the bulk has inverted, an ascending hole transient current is measured. When analyzing the electric field of an irradiated detector, one has to take into consideration that the measured signal is affected by the trapping of the charge carriers into the radiation induced defects. The influence of the trapping can be deducted by applying so called trapping correction method (CCM) [6,7], which is a mathematical manipulation of the measured raw data. The charge correction used in this content was performed by a Matlab program where the user defined input parameters are V_{fd} and the integration time of the recorded TCT signal. The charge correction is illustrated in figure 1.

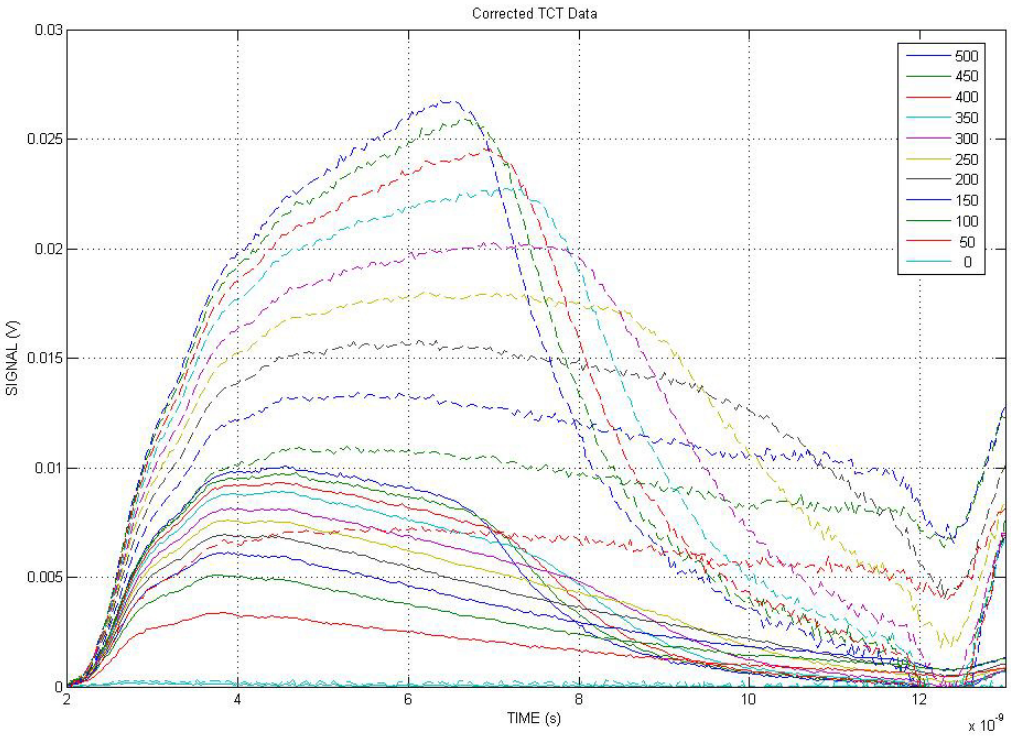

Figure 1. Measured (solid) and CCM charge corrected (dashed) TCT transients of irradiated detector.

The full depletion voltage can be determined from the TCT measurement either by visual inspection of the shape of the transient or by, more analytical method, integrating the charge with respect of bias voltage and extracting the charge saturation voltage value (QV method). In this study, the V_{fd} values were determined by the QV method. The principle of the QV method is illustrated in figure 2.

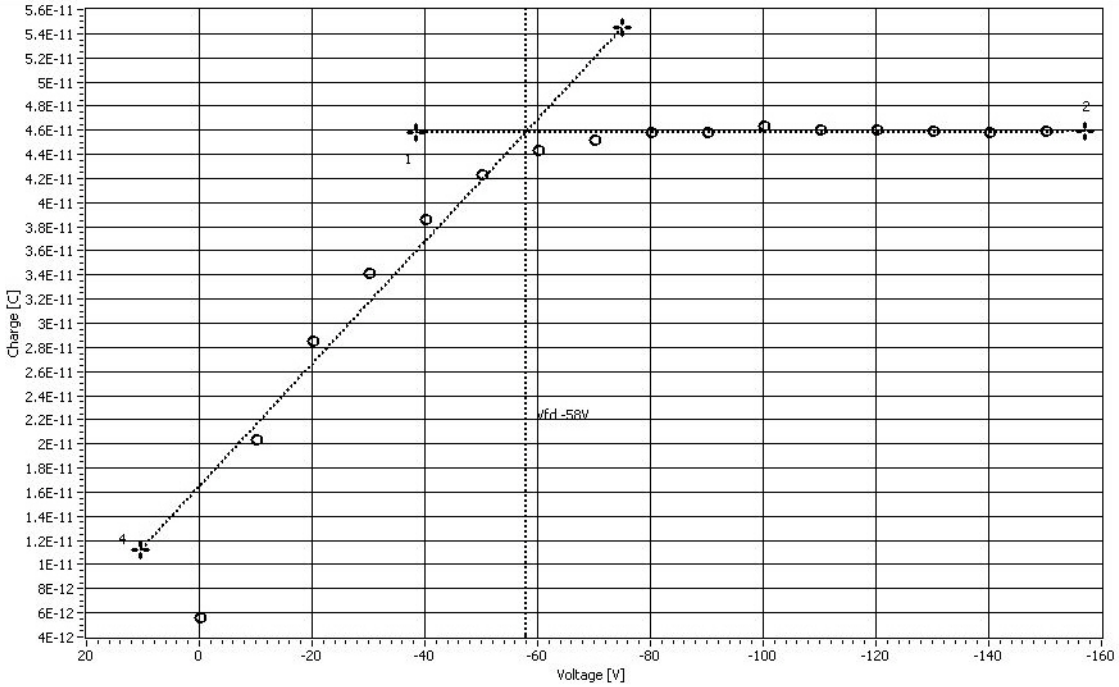

Figure 2. Fitting of the V_{fd} by QV method. The measurement temperature is 150K and the sample is thermal donor (TD) compensated $n^+/p^-/p^+$ MCz-Si detector. The extracted V_{fd} is 58V.

Our TCT setup consists of a 1 GHz bandwidth oscilloscope, a source meter unit capable to source up to 500 V, a vacuum chamber, a cold finger, a Stirling cryocooler, temperature and vacuum control units, lasers emitting 680 nm and 1050 nm light, and data acquisition and analysis software. The infrared (IR) laser is used for the simulation of minimum ionizing particles (MIP). The width of the laser pulse is about 30 ps (FWHM) and the maximum optical power is 250 mW. Very high optical power is needed for low temperature CCE measurements because the absorption of IR light decreases with respect of temperature as shown in figure 3.

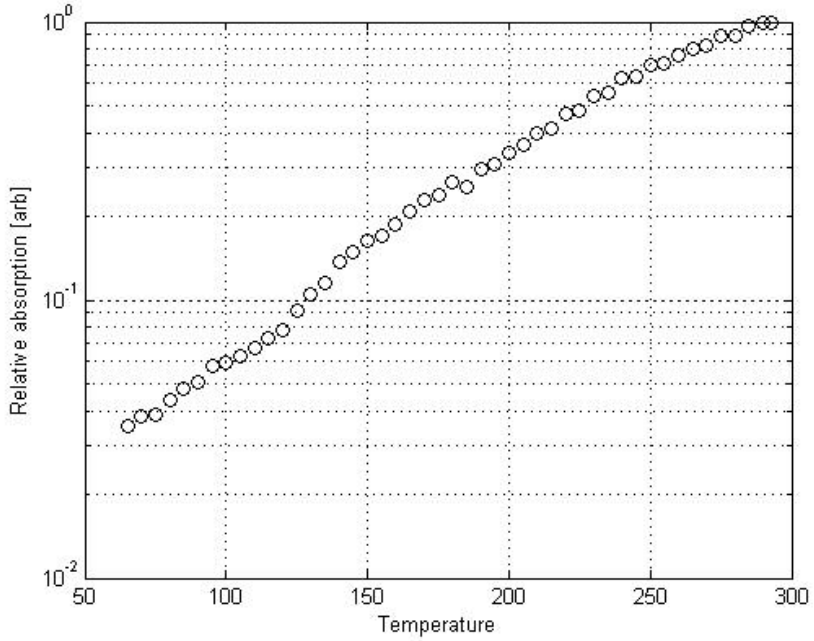

Figure 3. Relative absorption of 1050nm light in silicon as function of temperature. The measurement has been done by recording the total collected charge of an unirradiated detector.

The trigger rate of the lasers can be adjusted from 1 MHz to single shots. The biasing circuit, i.e. so called T-bias, of the setup consists of 33 kΩ resistor and 10 nF capacitor. The signal is amplified between the T-bias and the 50 Ω oscilloscope input by wide bandwidth amplifier developed by RD39 having a gain of approximately 120.

During the measurements, the lasers are operated typically at 10 Hz repetition rate while tuned to 60% of relative power. This is practical level of optical excitation in our system taking into consideration the reasonable signal to noise ratio. The low injection is preferred in order to minimize the polarization [8] effects at the cryogenic temperatures. Due to the mechanical design of the copper made cold finger, the diodes could only be illuminated on the front side.

The diodes were taped by double sided conductive carbon adhesive tabs on patterned gold plated ceramics. The ceramics have opening in the middle and a gold needle is soldered into the opening. The back contact that provides the high voltage is achieved by inserting the gold needle into a female coaxial connector in the gold finger. The pad contact and guard ring contact of the diodes were wire bonded into the gold metallization of the ceramics. Prior the measurements, the thermal contact between the ceramic and the cold finger are enforced by copper springs. Before the cooling of the cold finger, the vacuum chamber was pumped to 5×10^{-4} mbar pressure. To cool down the cold finger to 60K takes typically one hour with this setup. Every measurement took place only after the cold finger temperature saturated within 1 K of the set point. The temperature stabilization takes typically about five minutes. The detectors leakage current

was monitored during the temperature stabilization in order to ensure sufficiently small thermal gradient between the sample and the cold finger. The measurement arrangement is shown in figure 4.

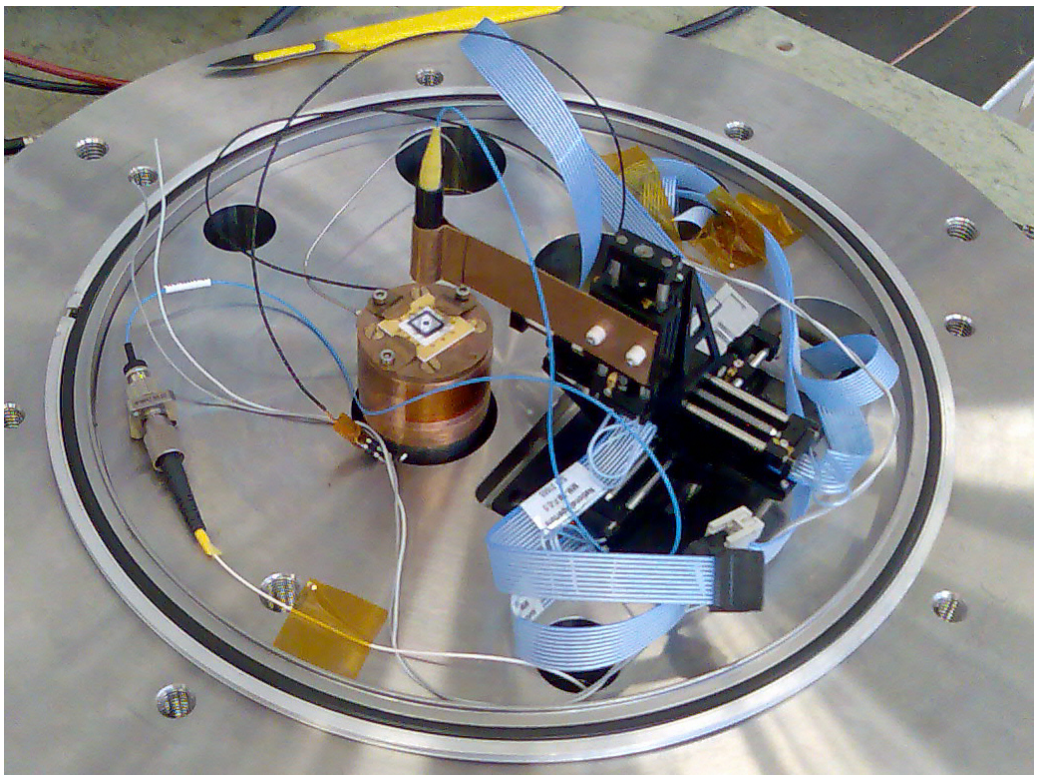

Figure 4. A gold plated ceramic with a bonded detector attached in the cold finger of C-TCT.

The IR response at 150K of C-TCT for irradiated and non irradiated detectors is shown in figure 5.

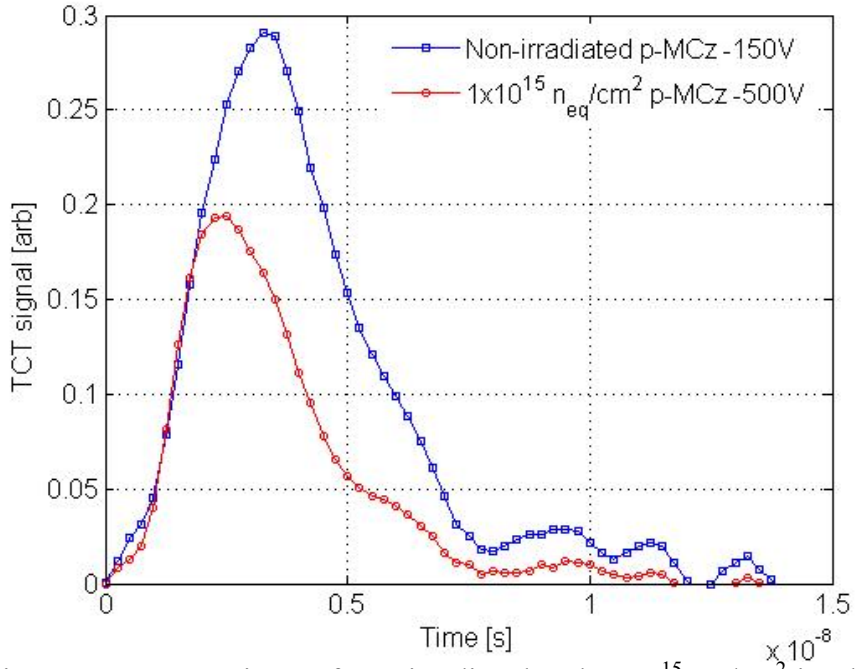

Figure 5. TCT transients of non-irradiated and 1×10^{15} n_{eq}/cm^2 irradiated $n^+/p^-/p^+$ MCz-Si detectors. The transients consists of both electron and hole currents.

The reverse bias voltage of non-irradiated detector is 150V, which is roughly 90V more than the V_{fd} as shown if figure 2. The bias on irradiated detector is 500V and it is below of the full depletion. It can qualitatively be seen in figure 5. that more than 50% of charge is lost due to the 1×10^{15} n_{eq}/cm^2 irradiation.

An example of the 670nm laser performance of C-TCT is shown in figure 6.

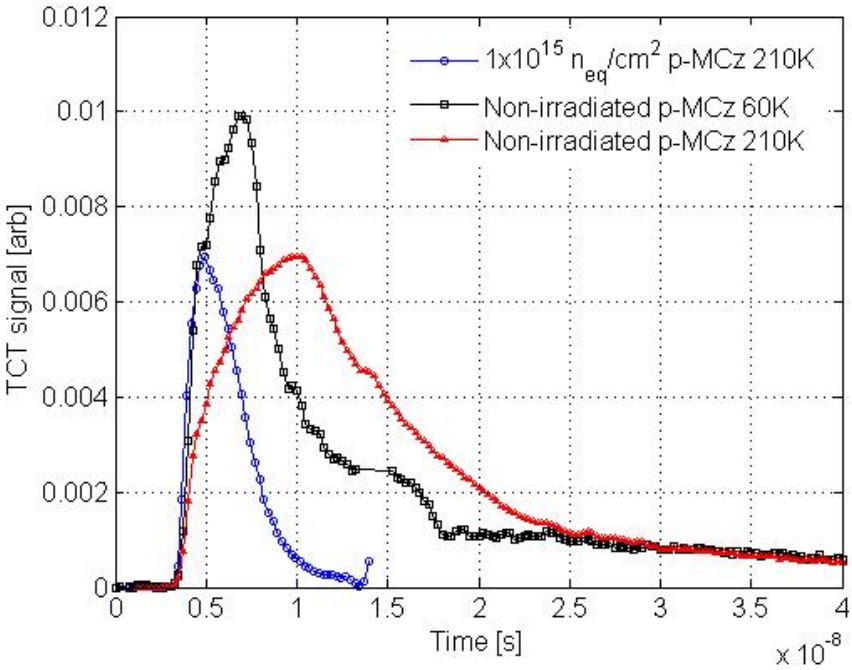

Figure 6. Hole current transients on non irradiated $n^+/p^-/p^+$ TD treated detector at 60K (red) and 210K (black), and proton irradiated 4×10^{14} n_{eq}/cm^{-2} (blue) diodes. The bias voltage is 150V for non-irradiated diode and 500V for the irradiated sample.

3. C-TCT measurements on p-type MCz-Si detectors at the low temperature

Recently intensively investigated approach to improve the radiation hardness of silicon particle detectors is to use $n^+/p^-/p^+$ structures instead of conventional $p^+/n^-/n^+$ detectors [9,10]. The essential advantage is that no space charge sign inversion (SCSI) occurs in p-type bulk, resulting in the collective junction to remain on the segmented side of the detector. In addition, the signal comes dominantly from electrons having three times higher mobility than that of holes and, consequently, the trapping of charge carriers within their lifetime (determined by the amount of particle radiation) is reduced. This allows higher charge collection in $n^+/p^-/p^+$ devices than in conventional detectors. Furthermore, if p-type Czochralski silicon is used as detector starting material, it is possible to tailor the full depletion voltage of the device by deliberate introduction of thermal donors (TD) [11,12,13]. TDs are complexes consisting of four or more oxygen atoms. Their formation takes place during the annealing of silicon wafers at 400-600°C [14], i.e. at temperatures that are frequently used during the detector processing. The drawback of $n^+/p^-/p^+$ devices is the more complex fabrication technology. Conventional detectors can be processed with 6-7 lithography mask levels while $n^+/p^-/p^+$ devices require two more levels and additional ion implantations.

The samples used in this study were pad detectors that were processed on p-type magnetic Czochralski silicon wafers (MCz-Si). The starting material of the detectors was 4“ diameter double-side-polished 300±2 μm-thick <100> Cz-Si wafers. The nominal resistivity, measured by the four point probe method, of the boron-doped wafers was 1800 Ωcm, which corresponds to a boron concentration of 4.38×10^{12} cm^{-3}. The processing and layout are discussed in detail in reference [15]. Two types of diodes were chosen for this study. First, diodes originating from a wafer that was sintered at 370º C for 30min (wafer ID p261). Second set with intentional TD introduction at 430º C for 45 minutes (wafer ID p047). The full depletion voltages of the diodes were measured by the capacitance-voltage (CV) method and were 300±10 V and 80±10 V, respectively. The pad leakage currents of all 0.25 cm^2 active area diodes were in the range of 1-2 nA. The surface current termination of $n^+/p^-/p^+$ devices was realized by p-stop implants.

The V_{fd} values, obtained by the QV method as function of temperature, are shown in figure 7.

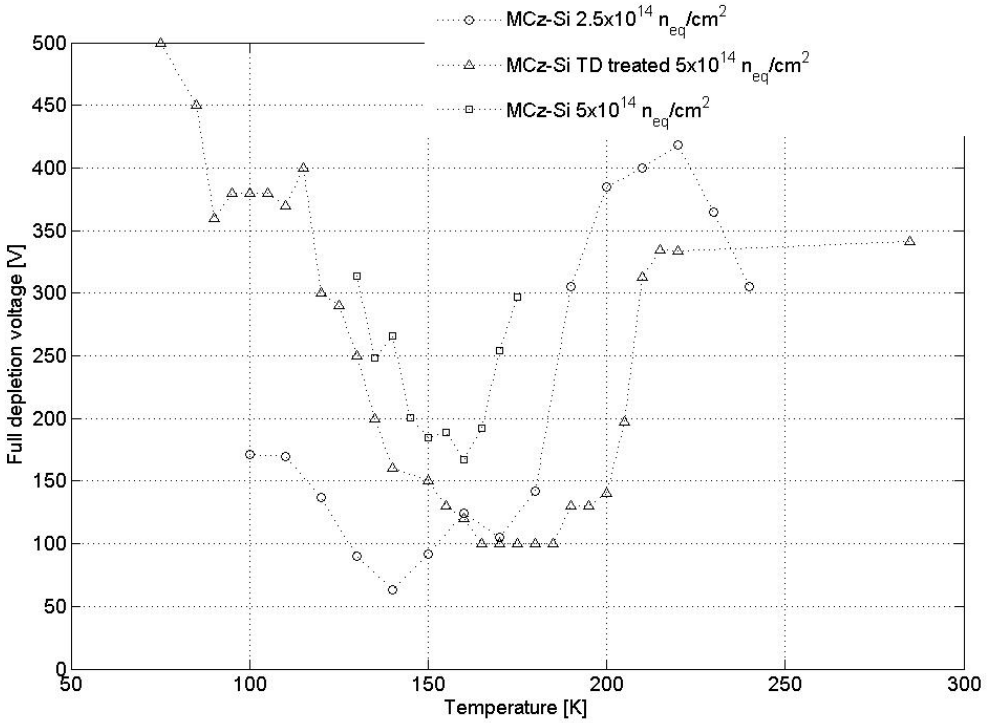

Figure 7.

As can be seen from the figure 2 in all three data point sets the V_{fd} reaches its minimum between 140 and 180K. The V_{fd} increases sharply when the temperature approaches 100K and also above 200K. The exception is the 5×10^{14} n_{eq}/cm^2 irradiated TD treated sample that could be fully depleted below 500V at 285K. The minimum of the V_{fd} of the non TD treated samples are about 80 V and 180V for 2.5×10^{14} n_{eq}/cm^2 and 5×10^{14} n_{eq}/cm^2 irradiated samples, respectively.

The extracted hole trapping time constant values as function of temperature are shown in figure 3.

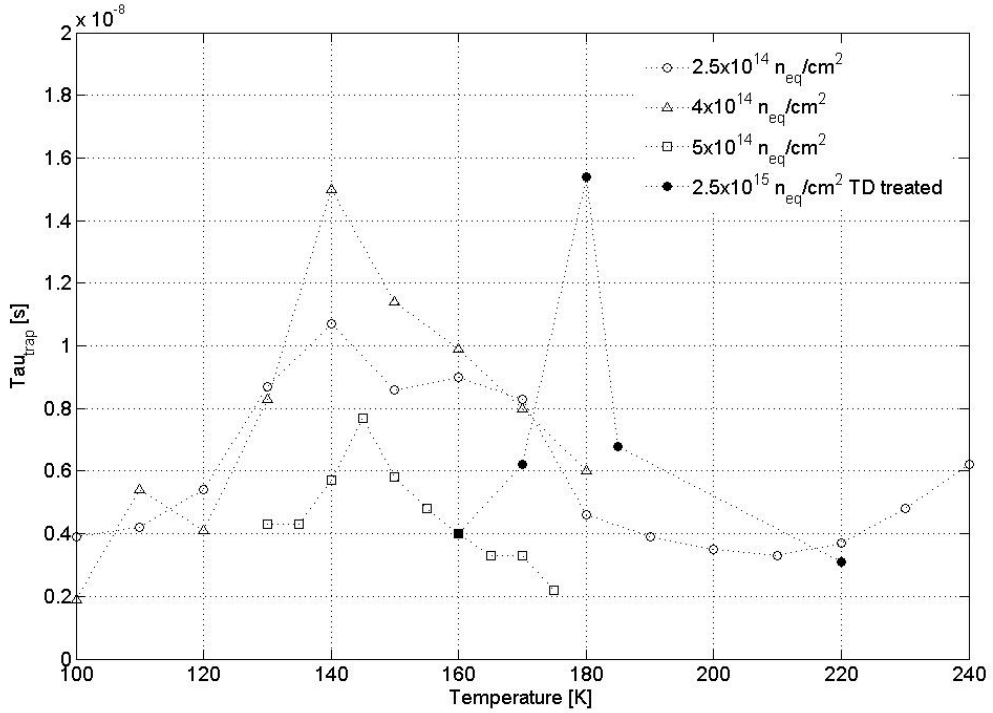

Figure 7. The hole trapping time (τ_h) vs. temperature.

Appositively to figure 6, the effective hole trapping time constant in all samples peaks between 140-180K. The hole trapping time (τ_h) values vary from 2ns to 15ns within the order of magnitude of the irradiation fluence. Also, the temperature dependence is strong. For example, in 5×10^{14} n_{eq}/cm^2 irradiated sample the τ_h is 8 ns at 145K and 2 ns at 175K.

Figure 8. shows the measured and CCM corrected TCT transients of 2.5×10^{14} n_{eq}/cm^2 irradiated non TD treated sample at 120K, 150K and 180K. According to the

figure 6. the V_{fd} minimum of this sample is at 140K.

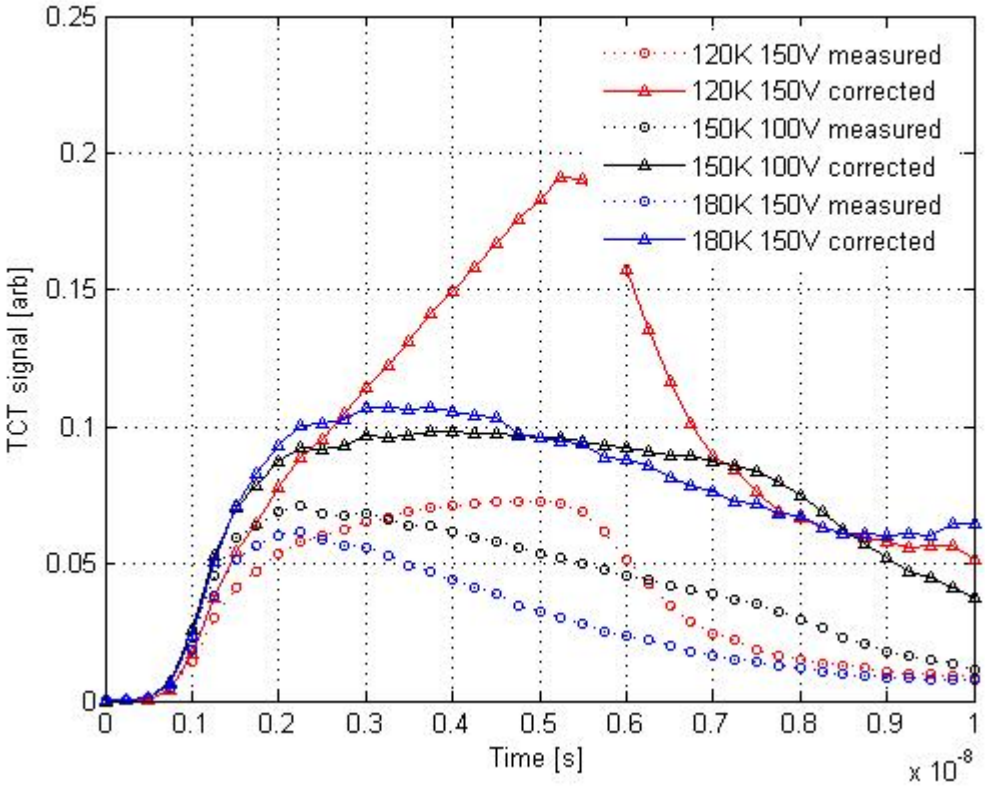

Figure 8. Measured and CCM corrected TCT transients at 120K, 150K and 180K of 2.5×10^{14} n_{eq}/cm^2 irradiated non TD treated MCz-Si diode.

Only smallest fluence samples could be fully depleted below 500 V at temperatures above 240K. At the low temperatures (<200K) it is apparent that SCSI occurs at certain temperature. This is due to the fact that the effective space charge is balanced by the trapping and detrapping. Trapping has no strong temperature dependence and it is inversely proportional to the concentration of trapping centers, while detrapping is exponentially dependent on the temperature. In other words, when a trap has absorbed an electron or a hole, it becomes neutral and does not contribute anymore to the N_{eff}.

4. The operation and performance of Current Injected Detector (CID)

If a detector with high concentration of deep energy levels is forward biased, the current is limited by the space charge. The current injection induces a stable electric field through the entire bulk regardless of the irradiation fluence the detector has been exposed [. So called “self-stabilized current injection” operation mode can be easily realized in the detector irradiated by the fluence higher than 1×10^{14} n/cm^2 and enables increased charge collection efficiency (CCE). Furthermore, because the electric field is established by

current injection, the detector operation is not sensitive on annealing of defects and CCE long term stability might be improved.

Our model for self-stabilized current injection (SSCI) CID operation is based on the physics of current flow in heavily doped insulators [4]. In a symmetric structure the holes are injected into the detector volume from the p^+ contact if a positive voltage is applied. The injected holes may be trapped by the deep levels, changing the effective space charge density (N_{eff}) and the electric field distribution ($E(x)$). The steady state density of the trapped charge is defined by the balance between the trapping and emission rates of holes (detrapping). Both rates depend on the concentration of the injected carriers and on the occupancy of the trapping centers. The local $N_{eff}(x)$ increases as a function of injected free carrier density, which is proportional to the current.

Next we consider the boundary condition at the positively biased contact. The p^+ contact is assumed to be a non-limited source of free holes. Formally, this condition would mean that the injecting contact could provide also current into the bulk. The mechanism of the current limitation and its stabilization is, however, due to the electric field deformation by the trapped holes. The trapped charge results in an increase of the electric field with respect distance from the the injecting contact. Obviously, at certain value of the injected current, the electric field $E(x=0)$ (or E_{inj}) will reach a value close to zero. Under these conditions an increase of the injection current density J_{inj} will be limited by the low value of E_{inj} and thus J_{inj} remains stable. This phenomenon is known as the Space-Charge-Limited Current (SCLC) and it has earlier been observed in insulators [17]. If charge diffusion effects are neglected, the electric field under steady state conditions at the injecting contact is $E(x = 0)$ zero.

The solution of the continuity and Poisson equations with Shockley–Read–Hall statistics for the carriers trapped by deep levels was performed by an iteration procedure with a MS Excel program. The iterative process solves the trapped charge density distribution at each value of injected current. The spatially resolved electric field was then used for calculation of the voltage, which is well-defined integral of $E(x)$ over the detector thickness. The figures 9 and 10 show the calculated $N_{eff}(x)$ and $E(x)$ at $T = 220$ K and 30 V bias for the symmetric p^+-n-p^+ silicon structure with a thickness of 300 μm. The deep level used in this calculation is a hole trap with an activation energy $E_t - E_V = 0.48$ eV. The concentration is $N_t = 2.8 \cdot 10^{12}$ cm^{-3}, which corresponds about 1×10^{14} n/cm^2 neutron irradiation. This value agrees with the introduction rate of about 0.02 cm^{-1}[18].

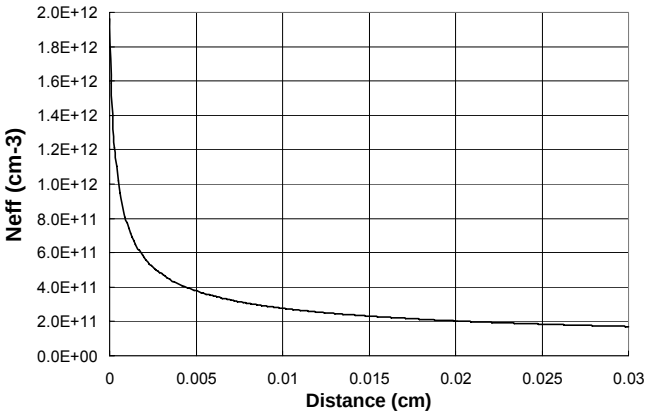

Fig. 9. Effective concentration calculated for CID with hole injection at: $J_{inj} = 1 \cdot 10^{-5}$ A/cm^2, $V = 30$ V, $N_t = 2.8 \cdot 10^{12}$ cm^{-3} and $T = 220$ K.

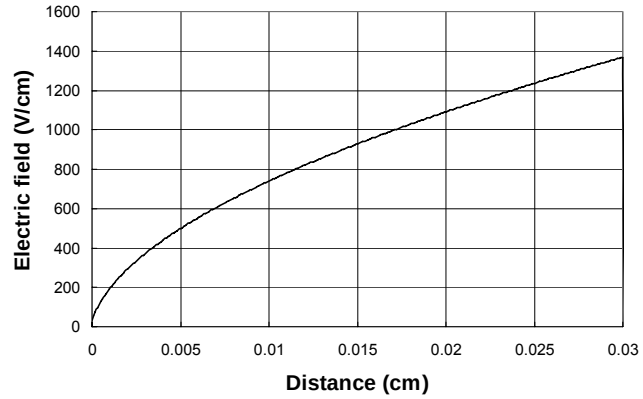

Fig. 10. Electric field distribution calculated for CID with hole injection at: $J_{inj} = 1 \cdot 10^{-5}$ A/cm^2, $V = 30$ V, $N_t = 2.8 \cdot 10^{12}$ cm^{-3} and $T = 220$ K.

The important feature of *E(x)* is that even at low forward bias the electric field extends over the entire detector thickness. The maximum of the electric field is at the contact opposite to the injecting contact. This means that the detector is fully depleted at any forward bias. This feature of the SSCI detector operation maintains the full depletion independently of the material properties. This in turn means that the electric field distribution is independent also on irradiation fluence. The calculated *E(x)* distribution at $V = 30$ V (Fig. 10) illustrates well this statement. Without current injection, in 1×10^{14} n/cm^2 irradiated high resistivity Fz-Si detector, the electric field would extend only 120 μm into the silicon bulk..

Simulated I-V curve of a CID operating in the SSCI mode is shown in Figure 3.

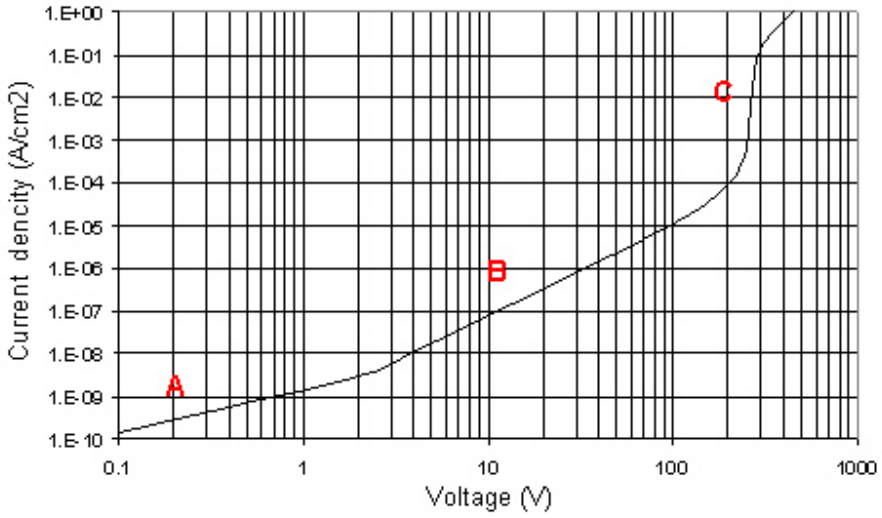

Fig. 11. Calculated I-V characteristic for CID. Parameters for the calculation are the same as in figures 9 and 10.

In the SSCI mode the I-V characteristic displays three major features. First, linear (ohmic) I-V dependence at low current (A). The low injected current cannot disturb the free carrier concentration n_0 in the detector bulk. Second, square law current voltage dependence (B). In the quadratic part the injected carrier concentration exceeds the free carrier concentration $n>>n_0$ and the current is limited by the space charge. Third, a sharp current rise at a certain bias voltage. The sharp current rise (C) at certain voltage (below threshold voltage (V_{th})) is a result of the deep level trap saturation (TS mode). This saturation prevents further self-stabilation of the trapped charge density to the increasing bias. In this case any increase of bias will lead to unlimited current injection until the injected free carriers themselves start to influence the electric field distribution. This will require $n>N_t$. It should be emphasized that the sharp rise of the current is not related to any breakdown effects.

In 2006 the CID IV characteristics have experimentally been verified by independent measurement by several RD39 groups. The IV measurements on CID's from

different producers made of different materials are shown if figure 12.

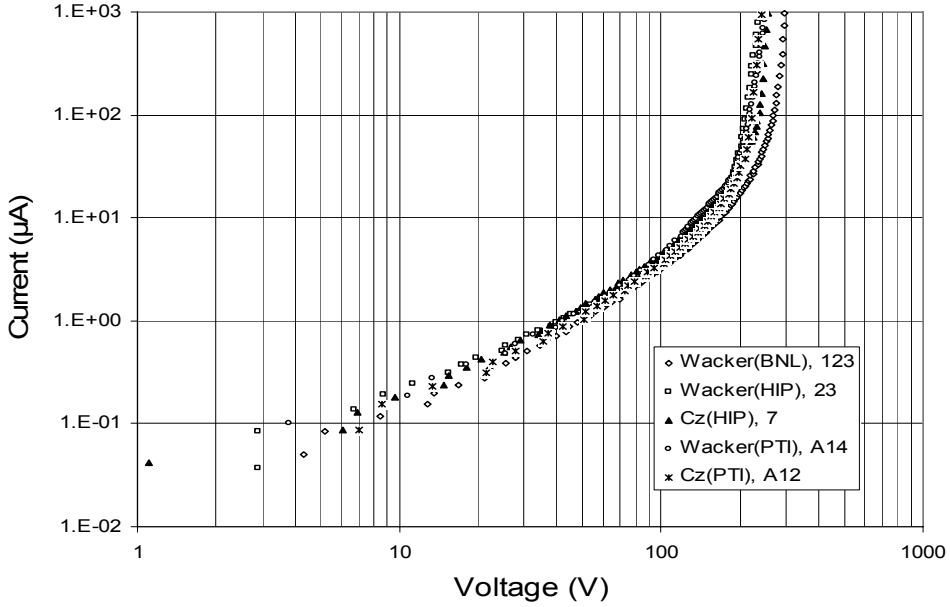

Figure 12. IV data of CID detectors processed at three laboratories; BNL (Brookhaven National Laboratory), HIP (Helsinki Institute of Physics), PTI (Polytechnical Institute Ioffe). Detectors have been made of standard Fz-Si and MCz-Si. The detectors have been irradiated by 1×10^{15} n_{eq}/cm^2 and the measurement temperature is 220K.

Figure 13. shows a family of IV curves measured at different temperatures. The CID detector has been made of MCz-Si and it has received 7×10^{14} n_{eq}/cm^2 fluence.

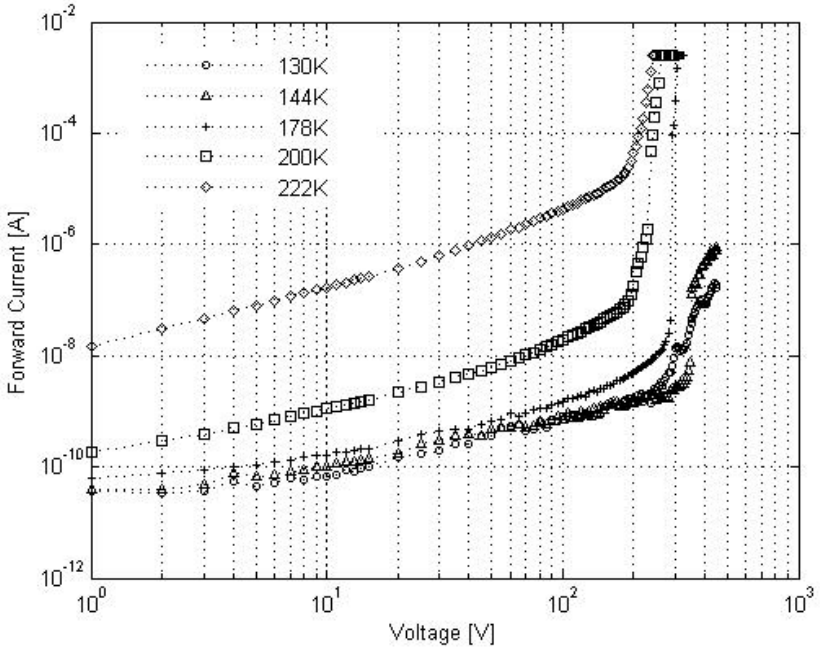

Figure 14. CID IV characteristic. The measurement has been performed at the Accelerator Laboratory of University of Helsinki [19,20].

The CID CCE measurement of the same device, which IV is shown in figure 14. is shown in figure 15.

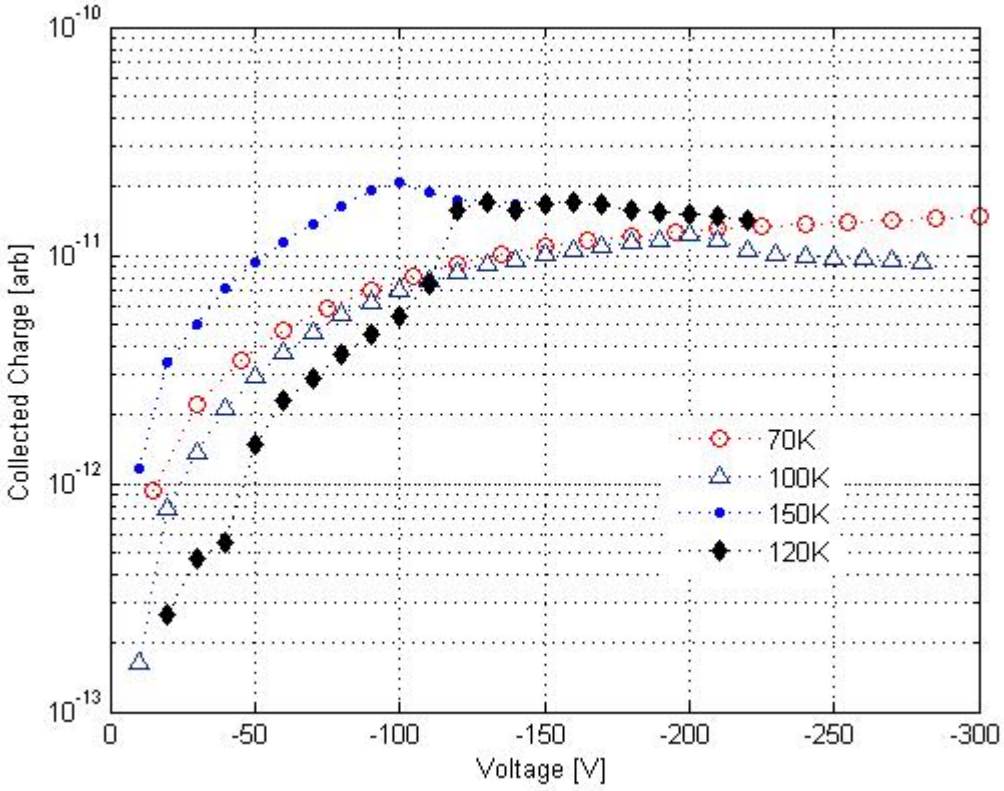

Figure 15. CCE measurement of 7×10^{14} n_{eq}/cm^2 irradiated MCz-Si CID detector. The measurement was done with 670nm laser by using RD39 C-TCT setup.

A comparison of charge collection efficiency between CID operation and standard detector operation is shown in figure 16.

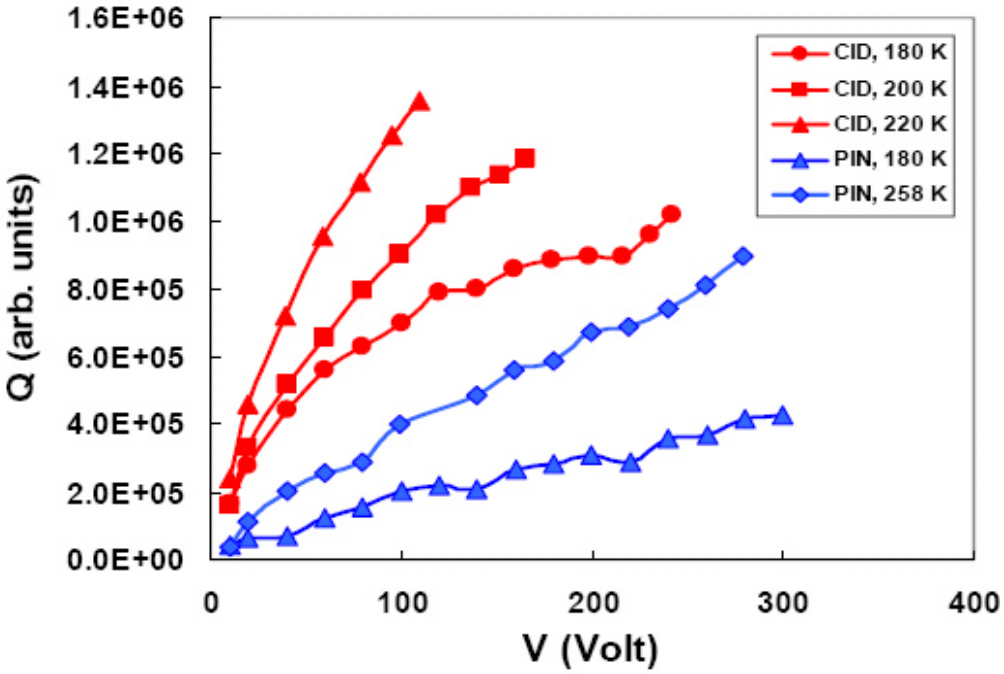

Figure 16. Collected charge of CID detector (red) and stardard pin-diode detector (blue).

The measurement shown above has been made by the TCT setup of PTI. The charge integration is done over a collection time of 15 ns that is close to the operational conditions in SLHC. The charge is presented in arbitrary units, which are the same for CID and reverse bias modes. For both modes the charge grows with bias voltage and temperature however the behavior of this growth is different. However, the CID provide signal up to 3.5 times higher compare with p-i-n detector at the same voltage and temperature. The CID operates at 220K ha advantages compare with p-i-n at 258K (operational temperature for inner tracker of ATLAS SCT experiment). The signal is up to 3.5 times higher at the same operational voltage. Even at the bias 300V p-i-n detector shows lower signal then CID at 100V. This illustrates an additional potential advantage of CID for application in the experiments – possibilities effectively operate even at the comparatively low bias voltage of 100-200 V.

To summarize other major advantages of CIDs for the operation at high fluences compare with regular detectors:

1) The geometrical factor of charge collection efficiency (CCE_G) is stable and is equal to one due to the electric field extension over the entire detector thickness at any fluence and bias voltage.

2) Long term stability of the collected charge of CIDs at any counting rates i.e. elimination of any polarization effect due to trapping of non equilibrium carriers.

3) Cheap manufacturing costs due to the simple device structure.

5. Low temperature Lorentz angle measurements at Karlsruhe

It is generally known that the drift of the charge carriers produced by charged particle transversion changes significantly under applied magnetic fields. Since the tracker systems in high energy physics experiments are located in high magnetic fields of around 4T, the drift of the signals' charge carriers produces an misalignment which has to be corrected due to magnetic field, and the affects to the Lorentz angels which are presented in the following. The results presented below have been measured on special double sided 128 channel strip sensors with 50µm pitch and a thickness of 500µm. The sensors have been irradiated by the 26 MeV protons to the 6×10^{13} p/cm^2 and 1.2×10^{14} p/cm^2 fluencies. After the irradiation the detectors were attached and bonded to the read out hybrid with Premux128 read out chip. The module is shown in figure 17. .

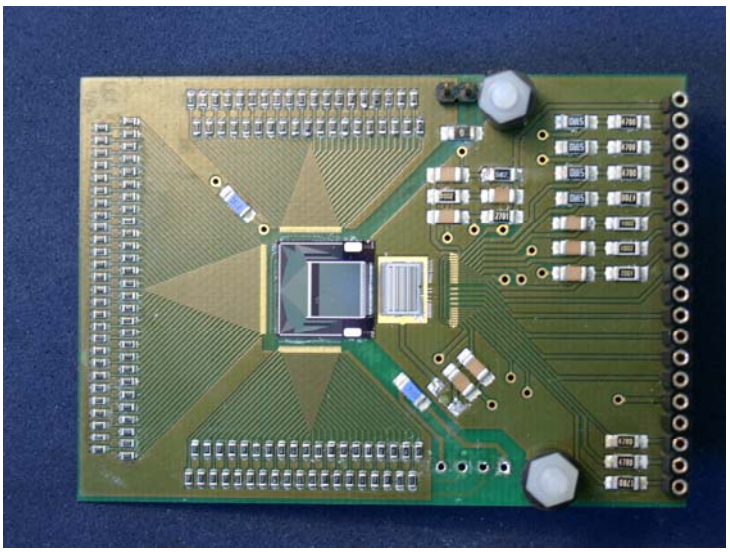

Figure 17. The detector module used in this study.

The measurements were performed at the setup equipped with red and infrared lasers, cryosystem capable to go down to the liquid nitrogen temperature and data acquisition system.
The following plots show the drift of the electrons and holes in non-irradiated reference detectors. The measurement was done by red laser light (660nm) at applied magnetic fields up to 8T.

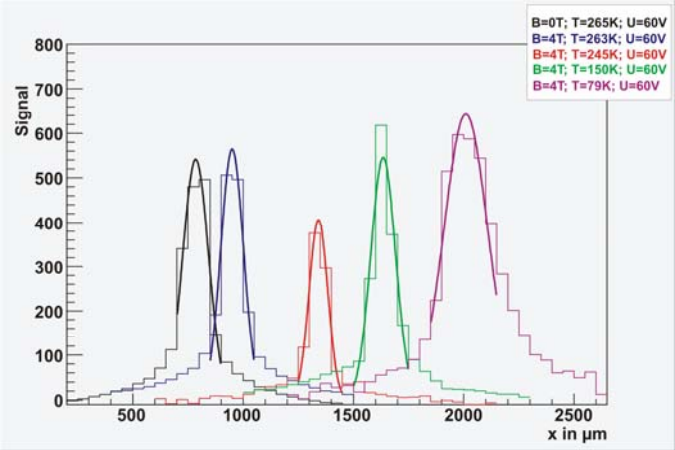

Figure 18. Displacement of electrons as function of magnetic field and temperature.

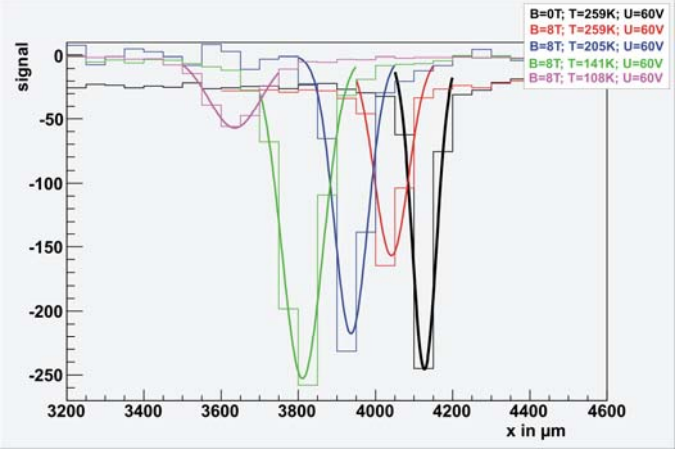

Figure 19. Displacement of holes as function of magnetic field and temperature.

The fluence dependence of the Lorentz shift is shown in figure 20.

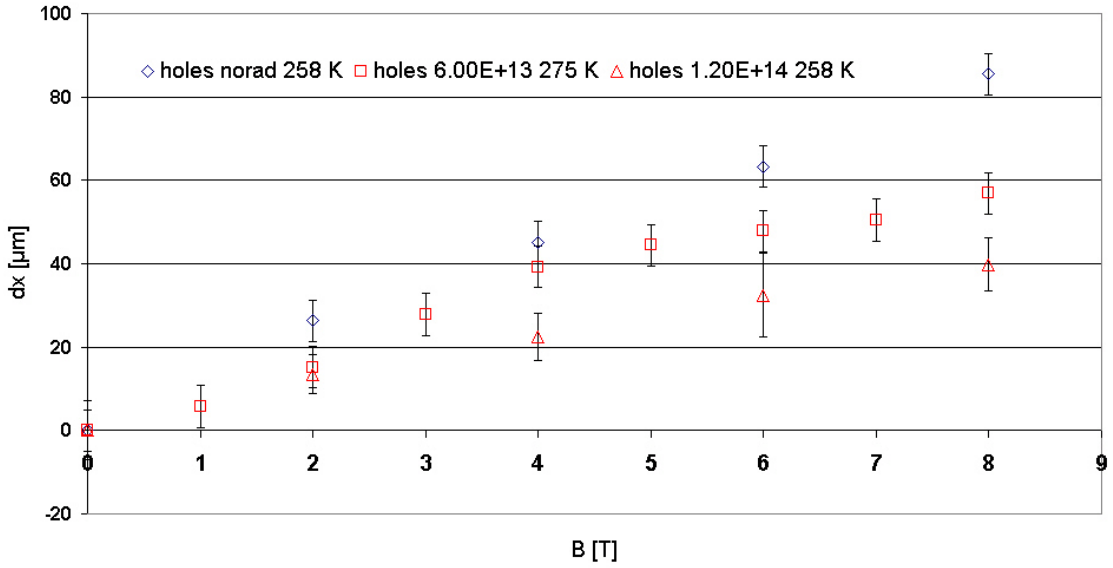

Figure 20. The displacement of holes in 6×10^{13} p/cm^2 (□) and 1.2×10^{14} p/cm^2 (◊) irradiated detectors.

The temperature dependence of the Lorenz shift is presented in figure 21.

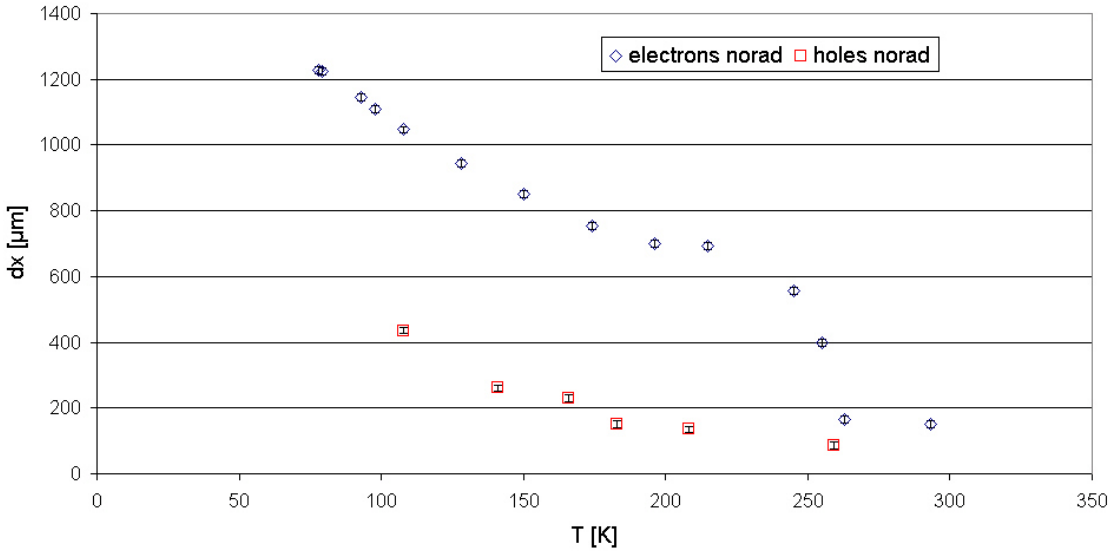

Figure 21. Lorentz shift for electrons (◊) and holes (□) with respect of temperature.

It can be seen in figures 18-21 that the Lorentz angle strongly depends on charge carrier type, temperature, and fluence. Since the first two parameters are expected to be caused by changes in mobility, the influence of fluence was not expected. A detailed analysis concerning the type of the defect will be investigated by the RD39 by Deep Level Transient Spectroscopy (DLTS) and TCT measurements.

6. Temperature dependent variations of the photoconductivity characteristic in proton and γ irradiated silicon

The photoconductivity decay under short pulse IR light excitation qualitatively and quantitatively depends on the trapping and recombination centers, therefore, these characteristics could serve as a fingerprint of the defects in the irradiated silicon.

Measurements of free carrier capture characteristics in the irradiated Si at different temperatures and analysis of models of the possible carrier decay processes to understand the details of the impact of the radiation induced defects.

Comparative analysis of the electrically active defects in starting and irradiated wafers as well as diode structures of silicon detectors material, varying irradiation parameters, by carrier lifetime temperature variations measured using the non-invasive contact-less techniques.

Three batches of samples were investigated. The first one was composed of homogeneous n- and p-type magnetic Cz (MCZ) Si wafers with dimensions of 20x20 mm^2 and of 300 μm thickness. The twin-samples of thermally treated and non-heated wafers were fabricated to control a role of thermal donors. These twin sample pairs were simultaneously irradiated with proton beam of 25 mm spot diameter. The 10 MeV and 50 MeV proton irradiations with fluences of $5x10^{12}$ and 10^{13} p/cm^2 as well as of $9x10^{12}$ and $2x10^{13}$ p/cm^2, respectively, were utilized. Thus, part of a wafer area was irradiated, that allowed to compare the characteristics of irradiated and non-irradiated material as well as to monitor homogeneity of irradiation. Surfaces of wafers of the starting material were passivated with thick thermal oxide films. TD processing of one of the twin-samples was made by 450 ^{0} C, 30 min heating in inert N_2 atmosphere. The second batch of samples consisted of pad-detectors fabricated on oxygenated n-type DOFZ Si, with introduced oxygen by a high-temperature 24 hours diffusion step, and non-processed FZ Si diodes for comparison. These detectors were irradiated by 24 GeV/c protons with $4x10^{14}$ and 10^{15} p/cm^2 fluences. The third batch of the MCZ sample pairs were irradiated with Co-60 γ-rays collecting a 50 Mrad dose. The carrier lifetime and Fourier transform infrared absorption spectroscopy (FTIR) investigations were performed on these 50 Mrad irradiated samples. Then, the irradiated non-heated wafers were cut in four pieces of dimensions 10x10 mm^2 and irradiated additionally with doses of 80, 160, 270 and 320

Mrad, respectively. A complementary sample of pad-detector, fabricated on n-type standard FZ Si and irradiated with 400 Mrad Co-60 γ-rays, was examined.

Excess carrier recombination transients were examined by combining analyses of the excess carrier decays dependent on the excitation intensity, on bias illumination and temperature, measured using the microwave absorption technique. Experimental setup and basics are sketched in Fig. 21. Excess carriers are generated in the bulk of the samples by either 1062 nm or 1064 nm wavelength light of the YAG: Nd^{3+} laser by using 30 ps, 500 ps or 10 ns pulses, and carrier decay transient is probed by microwaves (MW, at 10 or 22 GHz) sensitive to excess carrier density via free carrier absorption. Continuous wave broad band bias illumination (BI) was employed to suppress trapping by emptying/filling the capture levels. The samples were placed on cold/hot finger to measure the lifetime temperature characteristics from those the trap activation factors were deduced.

For deeper understanding of lifetime vs. temperature variations, carrier density relaxation transients have been complementary examined by combining MW probed PC with transient grating technique. Experimental setup and basics of the transient gratings technique are sketched in Fig.2. Transient gratings (TG) technique is based on the measurements of the light diffraction characteristics on the interference pattern induced dynamic grating of the spatial modulation of the material refractive index. Transient grating formation and erase is a function of the excess carrier density (ΔN) variations caused by carrier generation, recombination and diffusion. Transient grating is induced by interference field of the pulsed (30 ps) laser intersecting beams. Diffraction efficiency (η) on this grating is a measure $\eta \propto (\Delta N)^2$ of excess carrier density, while its variations in time $\eta(t) \propto exp(-2t/\tau_G)$ by changing a grating spacing (Λ) enable one to evaluate directly the parameters of grating erase $1/\tau_G = 1/\tau_R + 1/\tau_D$ through carrier recombination (τ_R) and diffusion $\tau_D = \Lambda^2/(4\pi^2 D)$ with D as a carrier ambipolar diffusion coefficient.

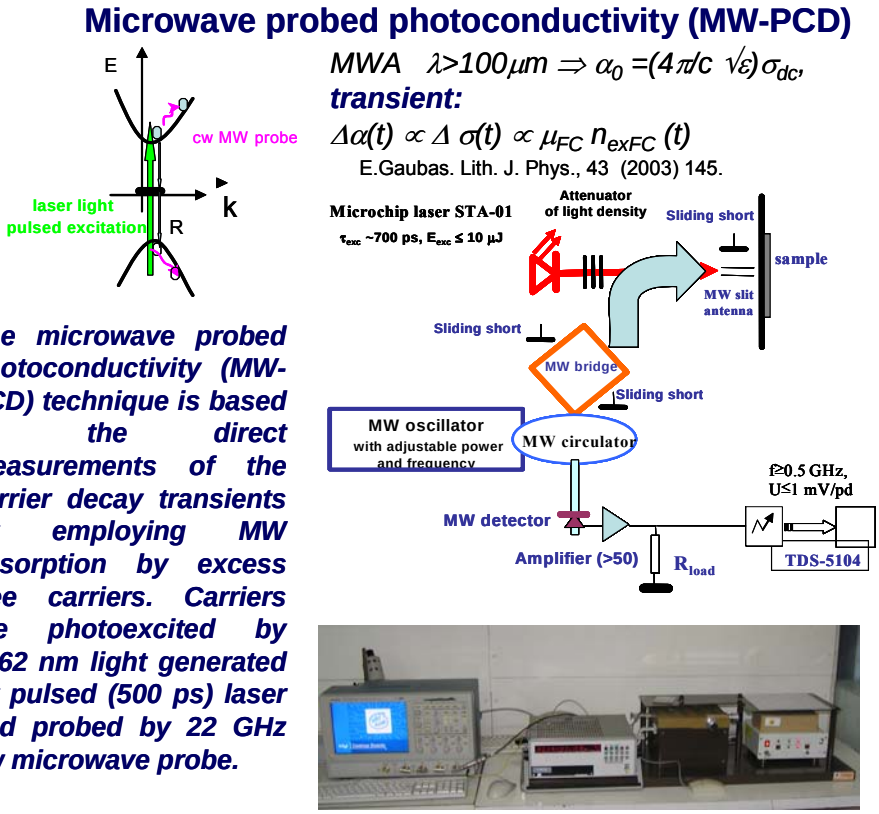

Figure 22. The MW-PCD measurement setup at the University of Vilnius.

Carrier lifetime (in the samples irradiated with a fixed fluence) variations with temperature have been investigated in a range of temperature between 90 and 450 K. These dependencies are illustrated for proton and γ-rays irradiated MCZ Si in Figs. 22a and b, respectively. Two peaks of carrier lifetime values were obtained in the ranges of low and elevated (above RT) temperature (Fig. 22a) in the proton irradiated material, while only a low temperature peak and a lifetime increase wing were observed in the γ-rays irradiated Si. The low-temperature peak is formed by trapping long-tail decay constituent. This peak appears together with an initial short component, when cooling a sample. This trapping constituent is nearly independent of BI (in the range of cw BI intensities applied). This lifetime increase peak is inherent for all the irradiated samples, while the absolute lifetime values vary in samples irradiated by different fluences, shown in Fig. 22a. In the starting material, these lifetime vs. temperature variations were not resolvable. Variations of the short decay component, which prevails in the irradiated samples at elevated temperatures, form the high-temperature peak, shown for one sample of n-type MCZ Si. The trap activation factors were preliminary deduced by using the lifetime as a function of 1/kT plots. In n-type wafers, the dominant traps with the effective activation energy of about 0.56 eV, 0.23 eV and 0.1 eV have been revealed by the simple analysis of the slopes within the carrier lifetime dependence on temperature. In the n-type DOFZ pad detectors irradiated with fluences of $4x10^{14}$ and 10^{15} p/cm^2, the dominant trapping level is characterized by activation energy 0.3 eV. In p-type MCZ Si

material, effective trap activation energy values of 0.4 eV, 0.19 eV and 0.1 eV were extracted.

In the γ-rays irradiated MCZ Si material, effective trap activation energy values of about 0.14 eV - 0.17 eV and 0.36 - 0.38 eV were extracted.

The oxygenation and heat treatments (TD process) probably introduce shallow levels (TD are characterized by the energy factors of 0.07 and 0.15 eV), and trapping centers with activation energy in the range of 0.1- 0.15 eV, determined from lifetime temperature dependences (Figs. 5a and 5b), can be attributed to TD.

The extracted trap activation energy effective values of 0.56 eV, 0.23 eV and 0.1 eV, can be attributed to di-vacancy and thermal donors after proton irradiations in the range of moderate fluences. In the n-Si pad detectors irradiated with high proton fluences of $4x10^{14}$ and 10^{15} cm^{-2}, the dominant trapping level is characterized by the activation energy 0.3 eV which may be associated with interstitials of Si_i and vacancy complexes. In proton irradiated p-type material, the extracted trap activation energy values of 0.4 eV, 0.19 eV and 0.1 eV can be attributed to di-vacancy, VO complex and thermal donors, respectively. In γ-rays irradiated material, the dominant trapping level, characterized by activation energy of 0.36 - 0.38 eV, may be associated with vacancies and VO complexes.

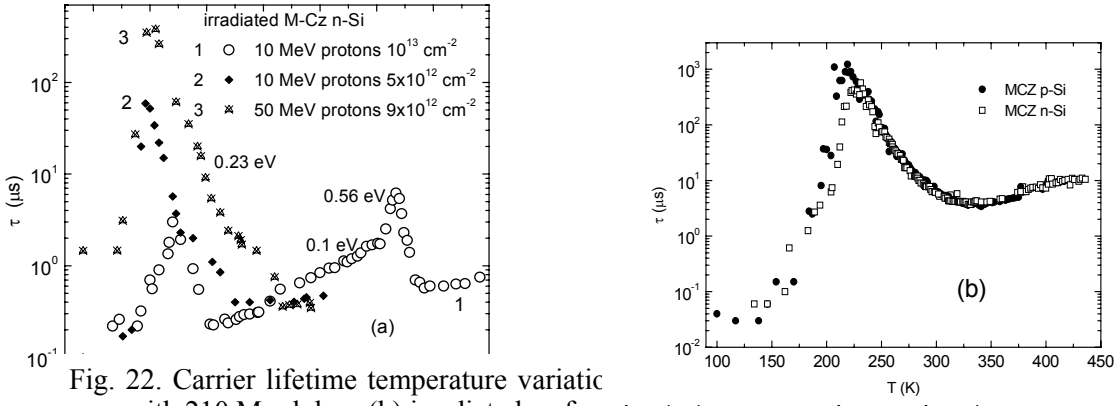

Fig. 22. Carrier lifetime temperature variatic
rays with 210 Mrad dose (b) irradiated wafers due to trapping and recombination.

The observed lifetime dependences on temperature (Fig. 22) can be explained by simultaneous interplay of several recombination and trapping centres, when the trapping effect is resolvable for trapping coefficients >>1 In the starting material wafers with small concentration of trapping centres *M*, the trapping peak in the lifetime temperature dependencies was non-resolvable for excitations applied. The $\tau_i - T$ peaks are nearly independent of BI in the irradiated material. Also, position of the peaks in T scale, attributed to deep levels in proton irradiated MCZ Si, is shifted to lower temperatures. Thus, these results, especially the decrease of lifetime values at low temperature, require the deeper consideration of the recombination characteristics.

Therefore, for deeper understanding of lifetime vs. temperature variations, carrier density relaxation transients have been complementary examined by combining MW probed photoconductivity measurements with transient grating technique. The intricate variations of the MW-PCD and TG transients have been obtained decreasing temperature of the samples. The two constituents are inherent for MW-PCD transients measured in

the irradiated detectors when trapping component shows non-monotonic variation with temperature. Surprisingly, the decay lifetime was found to be significantly decreased in the range of low temperatures. The diffraction efficiency also exhibits a significant decrease with temperature (Fig.23). However, the latter variations appeared to be dependent on the irradiation fluence and material preparation technology, i.e. thermal oxygenation level.

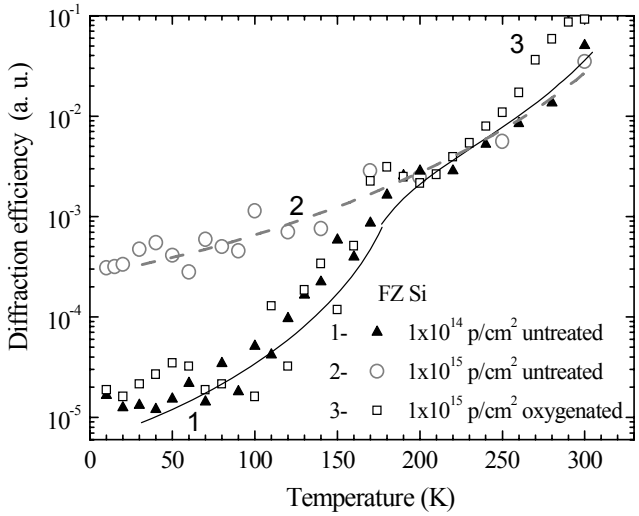

Fig.23. Variations of the diffraction efficiency on 1064 nm light induced TG with temperature in samples irradiated with protons of different fluences.

Temperature variations of carrier decay rate and of diffraction efficiency imply significance of the effects of trap filling/emptying and carrier generation by infrared light from deep levels. The increase of the diffraction efficiency on TG obtained in the heavy irradiated samples (curve 2 Fig.23) relatively to those containing less densities of point defects (curve 1 Fig.23) can be explained by additional (to the interband processes) generation of excess carriers from deep levels, as can be implied from absorption spectroscopy. The light emptied centers, then, are the fast capture levels, those are responsible for the decrease of carrier recombination lifetime in the range of the lowest temperatures.

Detail analysis of the lifetime-temperature variations. A simple approach of extraction of the trap parameters, discussed above, is relevant within phenomenological level for analysis of the clearly non-exponential relaxation transients. The initial τ_{in} and the asymptotic τ_{as} constituents can be taken as a measure of decay rates for the recombination processes and the trapping ones, respectively, within the previous simplified analysis.

More detail analysis has been performed by fitting the experimental lifetime variations with temperature by multi-exponential function. The latter analysis is implemented by fitting the decay curve using a sum of exponents and it corresponds to the case of low injection level when the partial constituents of the decay curve can be separated. The τ_{in}, τ_{as} and additional constituents of the multi-exponential function for the decay curves in Figs. 22b and 24 are listed in Table I. These lifetime constituents vary differently with changing excitation density, bias illumination and temperature. Variations of τ_{in} are rather small, while τ_{as} changes considerably with excitation regime

and temperature. The markedly non-exponential decay implies the competition between carrier recombination and trapping processes caused by several centers.

In reality, the τ_{in} might be also caused by the fastest processes during interplay of several traps. Further analysis is concentrated on the asymptotic (τ_{as}) lifetime. The last parameter is composed of several constituents, and impact of an intermediated fast process is revealed by fit of the experimental curves approximating the excess carrier density relaxation by a sum of three exponents. Only in the case of p-Si (sample A1) does the shortest constituent behave like a trapping center, i.e. the time constant decreases when the traps are filled by the bias illumination.

Table I. The constituents of the photoconductivity decay, shown as experimental curves in Fig.22b for heated (TD) and untreated (no TD) n-type MCZ starting material.

Decay curve	τ_{in} , μs	τ_{as} , μs	$y = A_1e^{(-t/\tau1)}+A_2e^{(-t/\tau2)}+A_3e^{(-t/\tau3)}$		
			τ_1 , μs (A_1 , a.u.)	τ_2 , μs (A_2 ,a.u.)	τ_3 , ms (A_3 , a.u.)
B1, BI off	1400 ± 27	3120± 36	23 ± 2 (11 ± 1)	861 ± 6 (66 ± 1)	3.12±0.04 (37 ± 1)
B1, BI on	1227± 24	2290± 25	19 ± 2(11 ± 1)	693 ± 4 (48 ± 1)	2.29±0.03 (55 ± 1)
B3 ,BI off	1890± 32	2417± 25		526±16 (21 ± 1)	2.42±0.03 (110 ± 1)
B3, BI on	1764± 35	2262± 28		619±16 (21± 1)	2.26±0.03 (107 ± 1)
A1, BI off	275 ± 1	49660± 190	10.5 ± 0.7 (21 ± 1)	180± 1 (98± 1)	49.7± 0.2 (20.1 ± 0.2)
A1, BI on	221±3	315±1	54.7±1.6 (33.4 ±0.5)	319±1 109±0.5)	

Table II. A set of the parameters exploited to have the best fit of experimental curves in Fig.22.

Sample	τ_R, μs	M, cm^{-3}	ΔE_M, eV	n^0, cm^{-3}	ΔE_R, eV	τ_0, μs	Trap for:
B3-50 Mrad	150	$7.0\ 10^{13}$	0.48	$1.0\ 10^{7}$	0.22	0.2	e
B1-50 Mrad	800	$2.5\ 10^{14}$	0.40	$7.5\ 10^{8}$	0.27	0.8	e
B1 210 Mrad	1000	$8\ 10^{10}$	0.56	$2\ 10^{6}$	0.17	0.035	e
B1 210 Mrad	1000	$2.5\ 10^{10}$	0.56	$1\ 10^{6}$	0.17	0.035	h
A1 210 Mrad	650	$5\ 10^{10}$	0.48	$8\ 10^{7}$	0.15	0.07	h
FZ-400 Mrad	180	$4.2\ 10^{12}$	0.495	$1.5\ 10^{6}$	0.18	0.04	e

The concentrations of recombination centres *R* and trapping centres *M*, estimated at the lowest excitation in the as-grown material, are less than 10^{11} cm^{-3}, and observed lifetimes are in the range of ms. In the starting material, the lifetime-vs-temperature variations were not resolvable due to the low concentration of grown-in centers. The low temperature peak in the post-irradiated samples is most probably formed by the long-tail

trapping decay component, which appears together with the initial, short component when the temperature is decreased.

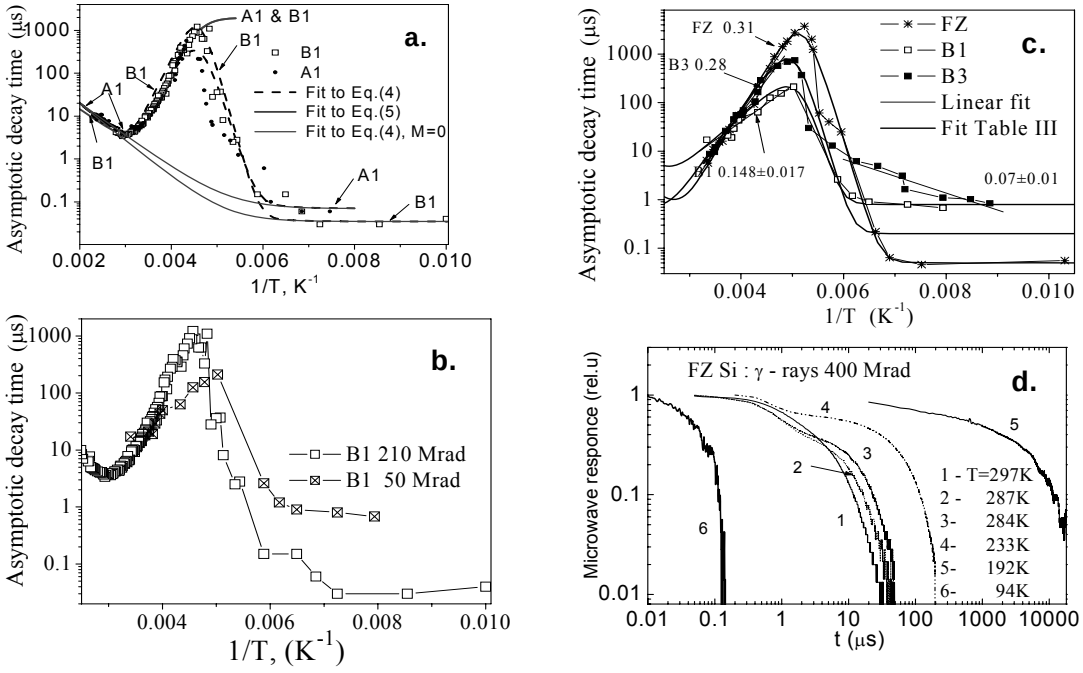

Fig. 23. (a) Carrier lifetime as a function of the inverse temperature in 210 MRad irradiated wafers of p-type and n-type MCZ Si at the same excitation conditions; (b) comparison of the carrier lifetime in the sample B1 after different levels of irradiation; (c) the asymptotic decay lifetime in 50 MRad irradiated wafers of n-type MCZ Si and in a 400 MRad irradiated FZ pad detector at different temperature and (d) the normalized MWA decay at different temperature in the irradiated FZ Si. The lines in (a) and (b) are the simulation results with the parameters presented in Table III. The dashed lines show the results if trapping is neglected. The inserts in (c) are the effective activation (quenching) energies. The errors (if not indicated) are of about 0.02 eV.

The simulations of the asymptotic time constant dependence on temperature, presented in Figs.7, are implemented by using a model of several recombination deep centers at assumption the fast traps dominate, when lifetime is expressed as follows:

$$\tau_i = \tau_R \left(1 + \frac{M N_{CM}}{\left(N_{CM} + n_i + n^0 \right)^2} \right) \exp(-\Delta E_R / kT) + \tau_0 . \qquad (1)$$

The parameters obtained for the best fit of the experimental curves in Fig.23 are given in the Table II. The best fit parameters appeared to be very sensitive to the activation and quenching energies those determine the asymptotic decay time constant and formation of lifetime peak position within temperature variation scale. The thermal activation of recombination τ_R lifetime should be included synchronously with that for trapping centers, accounted for within a N_{CM} parameter, to simulate the asymmetry of the asymptotic lifetime peak within its dependence on temperature.

The unexpected result is the significant decrease of the lifetime in the range of low temperatures, below 150K, and significant changes of the τ_{as} values over rather narrow segments of temperature variation. The wide-known centres in silicon are insufficient to explain the revealed features. Inter-centre recombination could be a reason for lifetime variations in highly irradiated material in the range of low temperatures, when tunneling plays an important role. For more comprehensive analysis, the defect clusters and configurational multi-stability of defects should be taken into account at low temperatures. The improved recombination-trapping model should be considered, if details of interplay of the recombination mechanisms at low temperature are confirmed. Then, instead of multiple trapping assumed within the analysis above, a "slow" trapping step should be incorporated (the pre-trapping before carrier recombination act). In the latter model, τ_{as} is defined by the thermal release, generation time constant:

$$\tau_{tr,g} = 1/\gamma_M(N_{CM} + n_0)\,. \qquad (2)$$

Continuing analysis within frame of this model, the data, presented in Fig 7a and Fig.7b for lifetime variations, would be ascribed to the trap thermal activation values, shown in the insets of Fig.23. Further, to fit experimental data, simulations are performed according to the modified Eq. 2, as

$$\tau_i = \tau_R exp(-\Delta E_R/kT) + 1/\gamma_M(N_{CM}+n_0), \qquad (3)$$

and the latter Eq.3 corresponds to the process when the lifetime is determined by the longest of time constants, determined by either the thermal activation or the recombination rate. Here, parameter γ_M denotes the carrier capture coefficient by the trap and it equals to $\sigma_M v$ with σ_M being the carrier capture cross-section, and v is thermal velocity. The fitting parameters are given in Table III.

Table III. The fitting parameters in Eq.(3) for the results presented in Fig. 23b.

Sample	ΔE_M, eV	$\gamma_M=\sigma v$, cm^3s^{-1}	n_0, cm^{-3}	ΔE_R, eV	τ_R, μs
B3-50 Mrad	0.28	$4\ 10^{-16}$	$2\ 10^{12}$		
B1-50 Mrad	0.14	$1\ 10^{-18}$	$1.5\ 10^{15}$		
B1 210 Mrad	0.38	$3\ 10^{-14}$	$1.7\ 10^{10}$	0.14	370
A1 210 Mrad	0.38	$3\ 10^{-14}$	$1.7\ 10^{10}$	0.14	370
FZ-400 Mrad	0.30	$3.5\ 10^{-15}$	$1.3\ 10^{11}$		

An approximation, obtained by using these equations 2 and 3, is in better agreement with the experimental curves than that performed by using Eq.1. However, both models need more sophisticated improvements to analyse the recombination processes and lifetime variations in the range of the lowest temperatures.

As a summary, the inverse lifetime variations, estimated from the MWA transients and ascribed to the recombination and the trapping processes, appeared to be nearly linear increasing function of the γ-ray irradiation dose, in MCZ wafers. This indicates dominance of the point defect formation. The extracted values of the carrier capture

cross-section, ascribed to the radiation induced centers, are consistent with those inherent for the singly charged repulsive centers.

The observed lifetime dependences on temperature have been explained by competing of the trapping and recombination processes. The native defects in the starting material for standard FZ and MCZ Si could be a reason for the observed differences within lifetime dependences on both the irradiation dose and the temperature.

References

[1] M. Bruzzi et al.; Nucl. Instr. and Meth. **A 541** (2005) 189-201.
[2] H.W. Kraner et al., Nucl. Instr. and Meth. A326 (1993) 350-356
[3] RD39 Status Report, CERN-LHCC-2003-060 (2003).
[4] V. Eremin, Nucl. Instr. and Meth **A372** (1996) 388-398.
[5] V. Eremin et al., Nucl. Instr. And Meth, **A372** (1996) 188.
[6] T. J. Brodbeck, et al., Nucl. Instr. and Meth **A455** (2000) 645.
[7] G. Kramberger, et al., Nucl. Instr. and Meth **A476** (20002 645.
[8] B. Dezillie, et al., Nucl. Instr. and Meth **A452** (2000) 440.
[9] RD50 Status Report 2005, CERN-LHCC-2005-034.
[10] G .Casse Nucl. Instr. And Meth, **A 487** (2002), 465-470.
[11] J. Härkönen et al., Nucl. Instr. and Meth. **A 552**, (2005), 43-48.
[12] J. Härkönen et al., IEEE Trans. Nucl. Sci. **52** (5), 1865 (2005).
[13] M. Bruzzi et al., J. Appl. Phys. **99**, 093806 (2006).
[14] Y. J. Lee et al., Phys.Rev.**B 65**, 085205 (2002).
[15] M. Bruzzi et al.; Nucl. Instr. and Meth.**A 568** (2006) 56-60.
[16] V. Eremin et al., IEEE NSS Conference Record, 2004 IEEE Vol. 3,16-22 (2004), 2003–2006.
[17] M. Lampert, P. Mark, "Current injection in solids", Academic Press, NY, London, 1970.
[18] V.Eremin et al., Nucl. Instr. and Meth **A 476** (2002) 537-549.
[19] S.Väyrynen et al., "Setup for irradiation and characterization of materials and Si particle detectors", Nucl. Instr. and Meth.A, article in press.
[20] J. Härkönen et al.," Results of Current Injected Detector (CID) measurements at the Accelerator Laboratory University of Helsinki", RD39 Workshop I-2006, June 2006, Prague, Czech Republic. Available at http://www.hip.fi/research/cms/tracker/RD39/php/home.php

Workplan 2006-2007

Schedule for the projects of RD39 in 2006 and 2007

Task name	2006				2007			
	Qtr 1	Qtr 2	Qtr 3	Qtr 4	Qtr 1	Qtr 2	Qtr 3	Qtr 4
Device Physics/ Basic Research								
Radiation of segmented (strip) Si detectors				X	XXX			
Improvements on the Cryo-TCT (C-TCT) by adding a floating power - Simulations of injection and E field.					XXX			
CID measurements at T<80 K for pad detectors by red and IR lasers			XX		XXXXXXXXXX			
CID measurements at T<80 K for strip detectors by red and IR lasers						XXXXXXXXXXX		
More detailed CID modeling				XX	XXXXXXXXXXXXXXX			
Simulations of injection and E field at cryogenic temperatures						XXXXXXXXXXX		
Modeling of trapping at CID conditions at low temperatures					XXXXXXXXXXXXXXX			
Cryogenic Modules								
Characterization of CID operation of irradiated strip detectors with read-out electronics			XXX		XXXXXXXX			
Laser cut and ICP Plasma etching of edgeless CMS baby strip detectors			XXX		X			
Assembly of modules with edgeless CMS baby strip detectors					XXXXXX			
Electrical tests of modules at low temperatures						XXX		
Irradiation of modules							XX	
Source and beam tests of irradiated modules								XXXX
ICP Plasma etching of edgeless detectors			XXX		XX			

Resources

Resources of the 15 institutes in RD39, planned for the projects of RD39 for 2007. For institutes involved also directly in the experiments, the resources for the construction of the final detectors are not included in the figures given for the budget and for the FTE manpower.

Institute	Authors	Device Physics	Basic Research	Cryogenic Modules	RD39 Budget (CHF/year)	FTE In RD39
U. Northeastern	5	x	x		5000	1.00
BNL	2	x	x	x	20000	1.00
CERN	2	x	x		2000	1.00
U. Florence	4	x	x		4000	1.00
U. Geneva	1	x		x	1000	0.15
U. Glasgow	2	x	x		2000	0.50
HIP Helsinki	4	x	x		20000	1.00
U. Helsinki	4	x	x		10000	2
U. Karlsruhe	7	x	x		5000	2.00
U. Louvain	3	x		x	20000	1.00
JSI Ljubljana	4	x	x		2000	0.50
U. Naples	3			x	2000	0.50
Ioffe PTI	3	x	x	x	10000	1.50
U. Turku	3	x	x		5000	0.60
U. Vilnius	7	x	x		10000	2.0
Total	54	14	12	5	113000	14.75